MIT Libraries | DSpace@MIT

MIT Open Access Articles

Update on the Micro-X Sounding Rocket payload

Massachusetts Institute of Technology

Update on the Micro-X Sounding Rocket Payload

E. Figueroa-Feliciano[a,b], J. S. Adams[c,d], R. Baker[c], S. R. Bandler[c,d], D. Dewey[a],
W. B. Doriese[e], M. E. Eckart[c,d], R. Hamersma[h], G. C. Hilton[e], U. Hwang[c], K. D. Irwin[e],
R. L. Kelley[c], C. A. Kilbourne[c], S. E. Kissel[b], S. W. Leman[b], D. McCammon[f],
P. H. H. Oakley[b], T. Okajima[c], R. H. O'Neal, Jr.[g], R. Petre[c], F. S. Porter[c], C. D. Reintsema[e],
J. M. Rutherford[a], T. Saab[h], P. Serlemitsos[c], Y. Soong[c], S. N. Trowbridge[a], P. Wikus[b,†]

[a]Department of Physics, Massachusetts Institute of Technology, Cambridge, MA 02139, USA;
[b]MIT Kavli Institute for Astrophysics and Space Research, Cambridge, MA 02139, USA;
[c]NASA Goddard Space Flight Center, Greenbelt, MD 20770, USA;
[d]University of Maryland, Department of Astronomy, College Park, MD 20742, USA;
[e]National Institute of Standards and Technology, 325 Broadway, Boulder, CO 80305, USA;
[f]Department of Physics, University of Wisconsin-Madison, Madison, WI 53706, USA;
[g]Department of Physics, Florida A&M University, Tallahassee, FL 32304 USA ;
[h]Department of Physics, University of Florida, Gainesville, FL 32611, USA

ABSTRACT

The Micro-X High Resolution Microcalorimeter X-ray Imaging Rocket is a sounding rocket experiment that will combine a transition-edge-sensor X-ray-microcalorimeter array with a conical imaging mirror to obtain high-spectral-resolution images of extended X-ray sources. The target for Micro-X's first flight (slated for January 2013) is the Puppis A supernova remnant. The Micro-X observation of the bright eastern knot of Puppis A will obtain a line-dominated spectrum with up to 27,000 counts collected in 300 seconds at 2 eV resolution across the 0.3-2.5 keV band. Micro-X will determine the thermodynamic and ionization state of the plasma, search for line shifts and broadening associated with dynamical processes, and seek evidence of ejecta enhancement. We describe the progress made in developing this payload, including the detector, cryogenics, and electronics assemblies.

Keywords: Supernova Remnants, Puppis A, X-ray, Transition Edge Sensor, Microcalorimeter, Sounding Rockets

1. INTRODUCTION

Micro-X is a sounding rocket payload that will fly the first transition-edge sensor (TES) microcalorimeter in space and obtain breakthrough science from high spectral resolution observations of extended X-ray sources. This payload has been in design and development for the last five years and is now built and undergoing integration; its first flight (designated μX-F1) will be in January, 2013.

The scientific payload consists of a Transition Edge Sensor (TES) microcalorimeter array at the focus of a flight-proven conical imaging mirror. Micro-X capitalizes on three decades of NASA investment in the development of microcalorimeters and X-ray imaging optics. Micro-X offers a unique combination of bandpass, collecting area, spectral and angular resolution. The spectral resolution goal across the 0.2–3.0 keV band is 2–4 eV Full-Width at Half Maximum (FWHM). The measured angular resolution of the mirror is 2.4′ Half-Power Diameter (HPD). The effective area of the mirror and filter optical system, 300 cm² at 1 keV, is sufficient to provide observations of unprecedented quality of several astrophysical X-ray sources, even in a brief sounding rocket exposure of 300 s.

Send correspondence to E.F.F.: E-mail: enectali@mit.edu, Telephone: 1 617 253 3097

[†]now at Fusion for Energy (F4E), Barcelona, Spain

Our scientific program will focus on supernova remnants (SNRs), whose spatial extent has made high-energy resolution observations with grating instruments extremely challenging. X-ray observations of SNRs with microcalorimeters will enable the study of the detailed atomic physics of the plasma; the determination of temperature, turbulence, and elemental abundances; searches for other processes such as charge exchange or signatures of particle acceleration; and in conjunction with historical data, full three dimensional mapping of the kinematics of the remnant. These capabilities will open new avenues towards understanding the explosion mechanisms of supernovae and their roles in element injection into galaxies, their evolution into SNRs, their interactions with their environments, and finally their roles as particle accelerators. For μX-F1 and μX-F2, we will observe the Puppis A bright eastern knot (BEK) and a Puppis A ejecta region.

With Micro-X, we have designed a versatile payload capable of providing high-resolution science and a testbed for new technology. Micro-X is an excellent vehicle for advancing the technological readiness of transition-edge sensor microcalorimeter technology in a real flight environment and aid in the understanding and development of future flight-qualified microcalorimeter systems for larger orbiting missions.

2. HARDWARE

We have designed and built an X-ray imaging spectrometer coupled to a grazing-incidence optic capable of high-resolution spectroscopy of diffuse, extended objects. In this section we begin by giving an update of the current status of our payload as we work towards the launch in January 2013. We then describe the subsystems comprising the Micro-X science instrument.

2.1 Micro-X Project Status Summary

Over the last two proposal periods we have taken the Micro-X payload from a paper concept to a space telescope currently in integration and testing (I&T). Engineering models and flight versions of the subsystems have been built and tested. Integration efforts uncovered a number of issues, large and small, that prompted redesigns or modifications of various subsystem parts. To provide the necessary time to implement these modifications, the launch date was moved to January 2013.

Although problems are a normal part of every technology development process going from a laboratory system to a flight system, they have taken longer than expected. Even so, as shown in Figure 2(left) we have
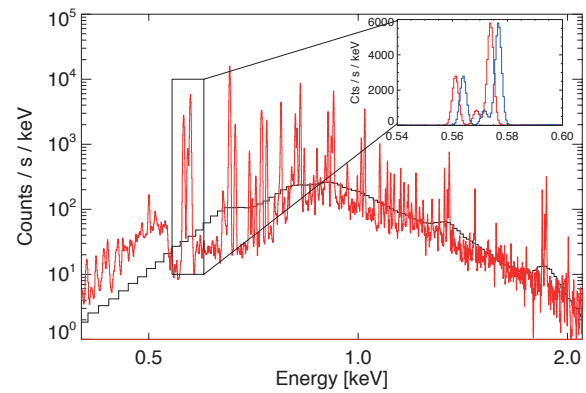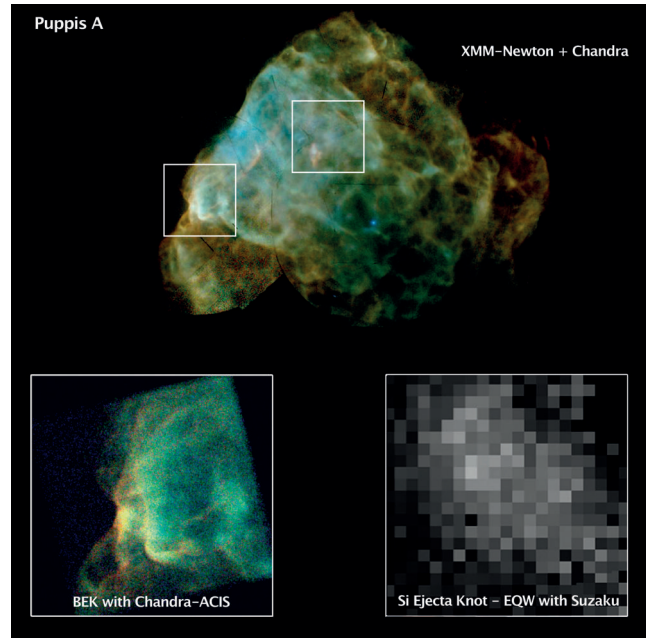

Figure 1. **Top:** Three-color image of Puppis A.[1] Red, green, and blue correspond to 0.5–0.7 keV (mostly oxygen K-shell lines), 0.7–1.2 keV (mostly Ne K-shell lines), and 1.2–5.0 keV bands, respectively. The boxes are the $11.8'$ Micro-X fields of view overlaid on the positions of the Si ejecta knot and the bright eastern knot (BEK). **Inset left:** *Chandra* ACIS image of the BEK, where the complex structure of the knot is apparent. **Inset right:** Equivalent width (EQW) image of the Si blend near 1.86 keV from the Suzaku Observatory that delineates the ejecta knot.[2] **Bottom:** Simulated Micro-X spectra from a 300 s observation of the Puppis A silicon knot region in red, with the Chandra spectrum in black. The inset shows the oxygen He-like triplet, clearly separable with 4 eV resolution. It also shows a 1500 km/s velocity blue shifted spectrum, showing the velocity resolution of the instrument.
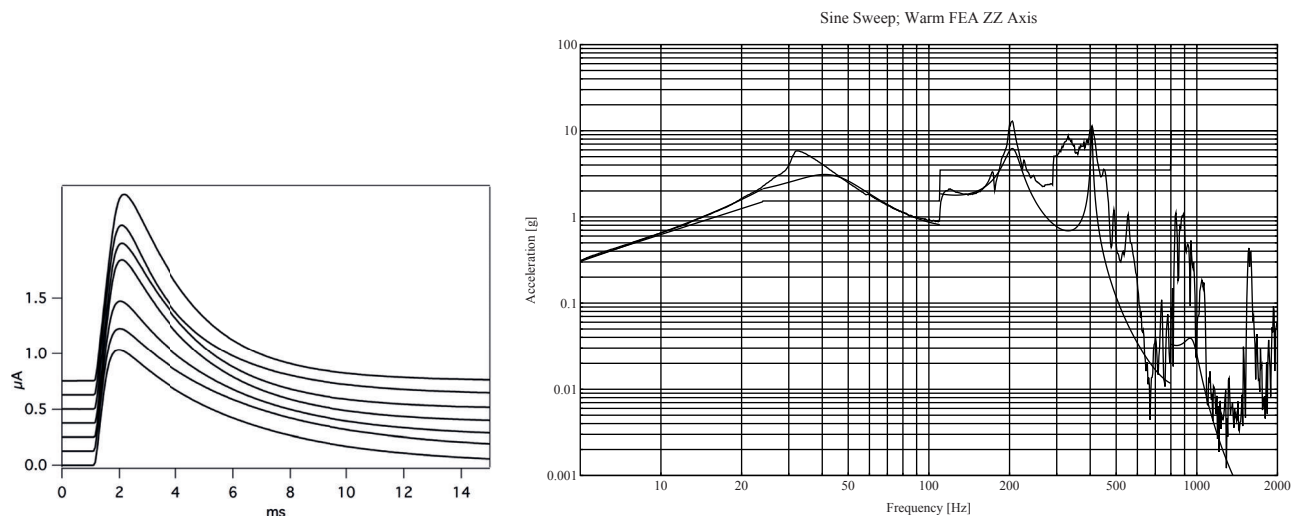
Figure 2. Left: Measured average pulse response from 5.9 keV calibration X-rays of seven Micro-X pixels. This multiplexed data is from the detector in the Micro-X flight cryostat and read out by the flight electronics. The pulses have been offset on the y-axis for clarity. Right: Data and model for room-temperature vibration test of the Micro-X flight cryostat. Dashed line is the input sine wave acceleration, gray solid line is the data collected from an accelerometer on the detector stage of the cryostat, and the black solid line is the best-fit curve for a 6-element single-axis vibrational model of the rocket and cryostat.

successfully integrated the detector system and are now taking pulse data on the flight cryostat, reading multiplexed TESs through the flight electronics and passing it through our Telemetry Simulator into our computers, testing the data path during actual flight.

We recently subjected the flight cryostat to vibration testing at the NASA Wallops Flight Facility. Both room-temperature and cryogenic tests were done, with full random vibe tests in the thrust axis. No mechanical failures occurred, all electrical connections, including those to the detector stage, magnet, and thermometry, survived the test without incident. We did see excessive heating of the detector stage during the cryogenic test, which we are investigating. The room-temperature sine sweep data for the detector stage is shown in Figure 2(right). The best-fit linear model with 6 masses representing the various components of the rocket skin / cryostat assembly is also shown. Good agreement is seen between the data and the simple linear model. Preliminary fits to the data point to a higher-than-desired resonant frequency of the cryostat, which is suspended from the rocket skin by vibration dampers. A resonance of the detector system between 300-400 Hz is not predicted in our model and is under investigation. Several minor modifications are possible that would change the resonant frequencies so as to minimize the heating of the detectors during launch. These are under evaluation and will be implemented soon.

I&T and Calibration will continue until November, when the science instrument will be shipped to Wallops Flight Facility for the pre-integration review (PIR) and full payload I&T. The payload will then be shipped to the White Sands Missile Range for launch in mid-January.

2.2 Payload Overview

The Micro-X payload consists of the science instrument, which has been developed and built by the Micro-X collaboration, and standard systems for telemetry, boost guidance, attitude control and payload recovery. These standard systems will be supplied by NASA. A CAD rendering of the entire payload is shown in Figure 3.

Micro-X successfully passed the NSROC design review in February 2010. Micro-X will be launched by a Terrier MK70 Black Brant MK1 (Mod 2) booster from the White Sands Missile Range. The total payload mass is 556 kg. The flight performance simulation determined that this configuration will reach an altitude of 283 km with 330 s above 160 km, some 10% more time than the 300 s estimate used in the science simulations.
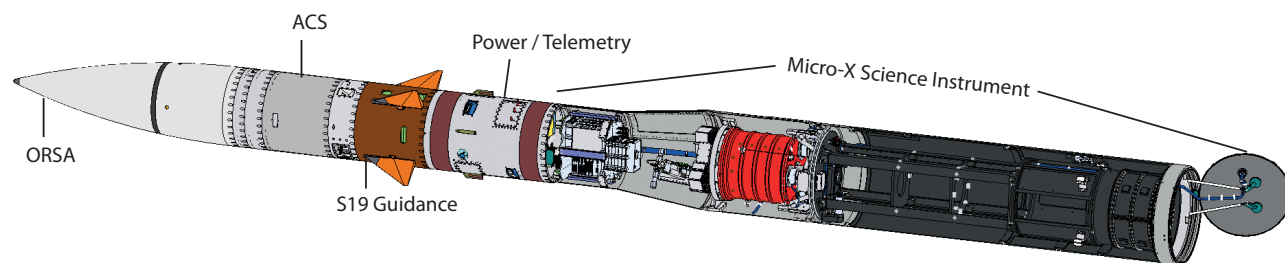
Figure 3. The Micro-X payload. The segments shown include the parachute recovery system (ORSA), the attitude control system (ACS), boost guidance, telemetry, and the science instrument.

2.3 The Micro-X Science Instrument Overview

Figure 4 shows the Micro-X science instrument and some of the fabricated hardware. The main components of the Micro-X science instrument are the avionics assembly (Figure 4b-c) for reading out the detectors and controlling the Adiabatic Demagnetization Refrigerator (ADR), the flight cryostat which houses the ADR and the TES microcalorimeter array (Figure 4e-g), the optical bench, and the X-ray mirror (Figure 4d). X-rays enter the system from the aft end of the payload. A shutter door sealing the payload is opened at an altitude of 95 km, once the two-stage rocket motor has been jettisoned.

Due to their respective diameters, the mirror, the optical bench and the ADR dewar are accommodated inside a 22 inch diameter skin. All other skin sections are 17.26 inches in diameter. The aft section, housing the optical bench and the X-ray mirror, is hermetic and can be evacuated before launch.

The ADR dewar is located in the vented section at the forward end of the instrument. The hermetic and the vented part are separated from each other by an aluminum bulkhead (Figure 4a), which is the main structural part of the instrument. X-rays can pass through the bulkhead from the mirror to the detector inside the cryostat through a valve in the center of the bulkhead. This valve is opened in space at an altitude of 160 km and allows the observation to begin.

Signals from the detectors are processed in multiplexing electronics in the avionics section at the forward end of the science instrument. The technical specifications of the Micro-X telescope and the entire payload are summarized in Table 1. The target energy resolution is 2–4 eV. Although 4 eV resolution is sufficient for the science measurements, the additional resolution allows tighter constraints to be placed on measured parameters, allows fainter lines to be resolved in the line-rich regions of the spectrum enabling elemental abundance mapping of less abundant elements, and aids in separating kinematically distinct components of the plasma through doppler shifts.

2.4 Detectors

Microcalorimeters are low-temperature photon or particle detectors. An absorber is connected to a low-temperature cold bath through a weak thermal link as depicted in Figure 5. When a photon is incident on the absorber, the photon's energy is converted into thermal energy causing the absorber's temperature to rise; it subsequently cools as heat flows out of the absorber and into the cold bath. The graph on the right of Figure 5 shows a typical "pulse" response, where the pulse height is proportional to the energy of the photon. Figure 2 shows actual responses from seven different detector pixels as measured in our flight system.

To obtain a precise measurement of the photon energy, we employ a sensitive thermometer to measure each temperature pulse. For Micro-X we use a TES as the thermometer element. A TES uses a thin superconducting film biased in its superconducting-to-normal transition, a region in which the film resistance has a very strong dependence on temperature. By applying the proper bias voltage to the TES, the device can be made to self-regulate in the very narrow transition and thus
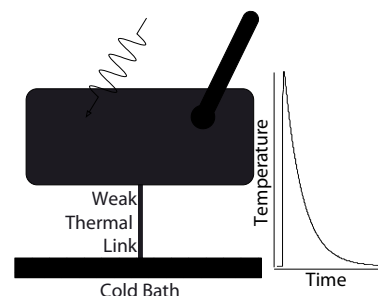
Figure 5. Schematic of a microcalorimeter.
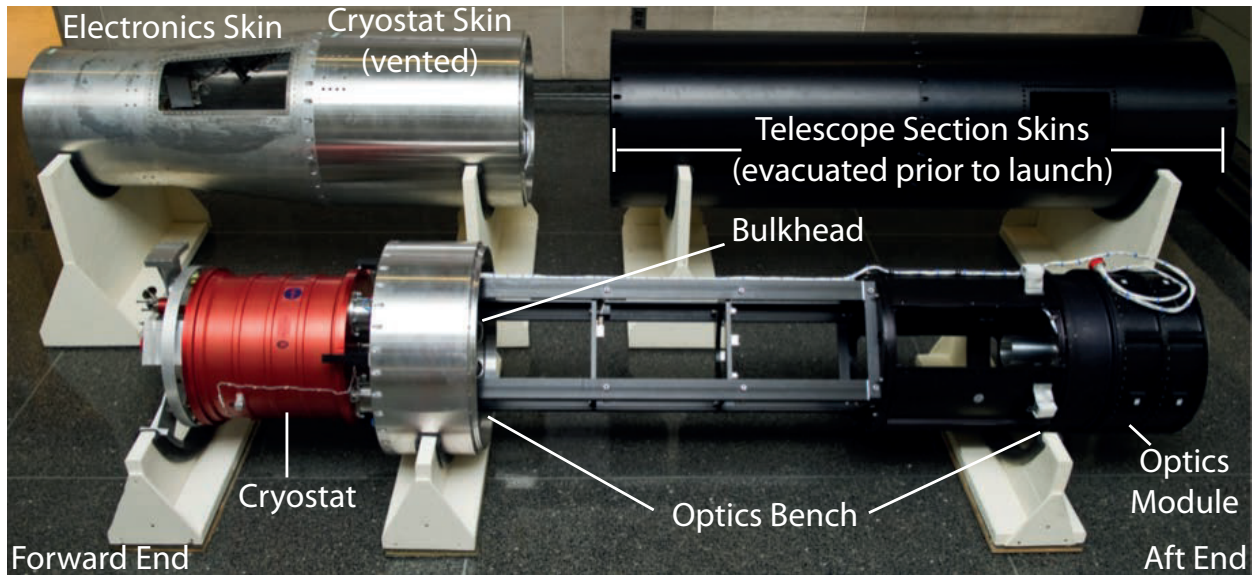
(a) Payload Overview including skin sections
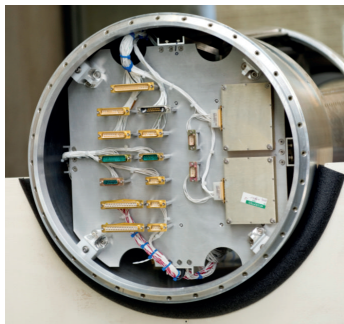
(b) Electronics Interface Plate
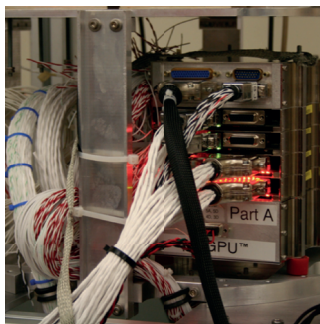
(c) Multiplexing Flight Electronics

(d) Flight Optics Module
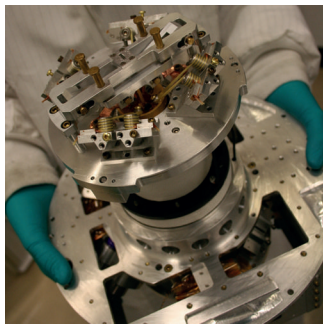
(e) Cryostat Flight Insert (magnet, heat switch, suspension system)
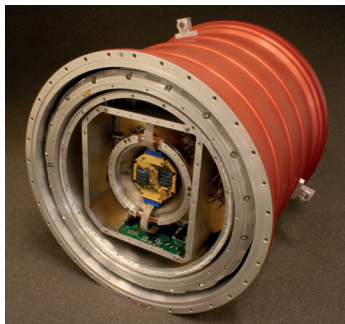
(f) Flight Cryostat (TES array and SQUID electronics)
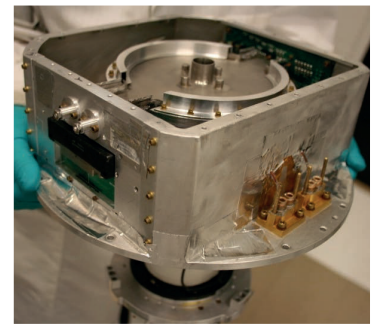
(g) Cryostat Flight Insert (thermal and magnet shields, science chain electronics)

Figure 4. Micro-X science instrument and some of the fabricated hardware.

Figure 3: The construction of the Micro-X science instrument flight hardware has been completed; the instrument is currently being tested and calibrated.

Energy Resolution	Target: 2–4 eV over science band pass
Operating Bath Temperature	Target: 50 mK
Detector Geometry	128 pixels in a quasi-circular arrangement (7.2 mm diameter)
Pixel Size	590 μm × 590 μm
Band Pass	0.2–3 keV
Effective Area	300 cm^2 @ 1 keV
Point Spread Function (PSF)	2.4 arcmin HPD
Focal Length	2100 mm
Field of View	11.8 arcmin (0.98 arcmin per pixel)
Payload Length	7.9 m
Payload Diameter	22 in (optics section) and 17.26 in (avionics and service systems)
Payload Mass	556 kg
Booster	1st Stage: Terrier MK70, 2nd Stage: Black Brant VC MK1
Time Above 160 km	330 s
Apogee	283 km
Attitude Control System (ACS)	GLN-MAC gyro and flight computer; celestial ACS with ST-5000 star tracker and bi-level cold gas thrusters
expected pointing stability	∼10 arcsec FWHM
Telemetry	Three independent S-band TM links (1.5 Mbit/s WFF-93 PCM encoder for housekeeping and two 20 Mbit/s MV PCM encoders for science data).
On-board Data Storage	16 GB
Power for science instrument	Batteries with a total capacity of 21.4 Ah @ 28 VDC

Table 1. Technical specifications for the Micro-X science instrument and payload.

create very high temperature sensitivity. TES microcalorimeter arrays have successfully achieved X-ray energy resolutions of < 2 eV Full-Width at Half-Maximum (FWHM) for arrays containing up to 1024 pixels.[3–6]

2.4.1 Detectors for Micro-X

The Micro-X array design consists of a 128-pixel array of 0.59 mm × 0.59 mm pixels on a 0.6 mm pitch giving a 97% fill fraction and essentially 100% quantum efficiency in the 0.2–3.0 keV bandpass. Coupled to the 2.1 m focal-length mirror, the plate scale is 0.98′ per pixel providing an 11.8′ field of view.

Figure 6 shows a photograph of one of the flight-candidate detector arrays. The Au/Bi X-ray absorbers sit in the center of the silicon chip. The absorbers can be readily integrated into the fabrication process to provide optimum heat capacity and X-ray opacity. Of the 144 pixels, 16 of the corner pixels will not be read-out during flight, since our electronics chain is designed for an 128-element array. The oval and triangular shapes at the left of the chip are through holes in the silicon to enable our kinematic mounting scheme (see §2.6.2).

Hidden underneath each of the absorbers is a TES made from a Mo/Au proximity-effect bilayer that is 250 nm thick and 140×140 μm^2 in area. Each TES sits on a thin SiN membrane, which acts as the weak thermal link between the device and the surrounding silicon (the cold thermal sink). Five posts sit on the SiN membrane and/or TES and mechanically support the overhanging X-ray absorber. Aside from these five absorber-contact regions, the absorber is on a plane several microns above the plane of the TES, wiring, and substrate. Figure 6 shows the corner of one of the pixels, where the absorber is cantilevered above the substrate.

We have successfully fabricated flight-candidate arrays and additional spares and test arrays. We have arrays with various superconducting transition temperatures (T_c's) so that we can choose an array that will match the best-achievable performance of the flight dewar (see §2.6.1). The array that has demonstrated the best spectral performance, $\Delta E_{\mathrm{FWHM}} \approx 3$ eV at 1.5 keV, has $T_c = 71$ mK and requires a bath temperature of $T_b = 50$ mK. An alternate array with $T_c = 120$ mK has a resolution of ≈ 4 eV and only needs to be cooled to $T_b > 70$ mK to achieve this performance.

The detector array will be housed in the Front-End Assembly (FEA; see §2.6.2), which provides mechanical and thermal staging of the TES array and the front-end SQUID amplifiers.

2.5 Readout Electronics

TESs are usually read out with superconducting-quantum-interference devices (SQUIDs). An inductively-coupled SQUID current amplifier is well-matched to a TES, both because of its low noise and its low input impedance. The conventional readout scheme for a single TES detector employs a single SQUID, connected to a series array (100 SQUIDs in series), which amplifies the signal to a level at which it can be handled by room-temperature electronics. A SQUID multiplexing scheme reduces the number of wires (and thus the heat load) to the detector stage, easing the requirements on the cryogenic system. NIST has developed a time-division SQUID multiplexing (TDM) architecture to read out large arrays of TESs.[7–9] For Micro-X, the Co-I teams at NIST and GFSC have developed a 64-channel TDM SQUID MUX system consisting of 4 readout columns, each reading out 16 detectors. Two fully independent readout systems are implemented to read out the 128-pixel detector array. These separate readouts also have separate power supplies, and go to separate telemetry systems. Thus two completely independent science chains take signals from the detectors to the telemetry. This design mitigates risk as a complete failure of a readout system would result in only half of the detector data being lost.

Each of the four readout columns in each science chain has its own NIST 1-column multiplexer chip, which has 33 first-stage SQUID rows.[7] Only 16 rows per chip are used. A specially designed NIST four-channel SQUID series-array module (based on previous work[10,11]) amplifies the column signals to a level that is well-matched to our room temperature electronics.

Figure 6. **Top:** The Micro-X detector array chip. The chip dimensions are 19 mm × 15 mm. **Bottom:** SEM of the corner of a pixel.

NIST designed and built the room-temperature electronics, which include the final amplification stage and digital sampling of the column readout and the digital feedback and row-switching drivers. The core of the system is the digital-feedback card. A row-address card switches the first-stage-SQUID bias signals synchronously with application of the feedback signal. A bias card based on the row-address card provides DC bias functionality for the SQUIDs and TES detectors.

GSFC has developed the Master Control Board (MCB). The MCB has several tasks; it handles the science chain system control, receives and processes both the science data and instrument housekeeping data, handles the on-board storage of the data as well as provides the data stream to the telemetry system on the rocket. Additionally the MCB also provides the Ground Support Equipment (GSE) interface to the instrument. There is one MCB for each 64-channel science chain.

The science data passes through the MCB, which records the full data stream (~ 66 Mb/s per science chain) to on-board flash memory, allowing for subsequent analysis of the complete data set. The MCB will also send a downsampled version of the data stream to the telemetry system of the rocket, which has a bandwidth of ~ 20 Mb/s per science chain. Data from 60% of the pixels will be sent down through the telemetry, although all pixels are stored to on-board flash memory. Pictures of an operational MUX stack with feedback, row address and MCB cards are shown in Figure 4c.

2.6 Cryogenic Systems

The Micro-X cryogenic system is in a mature state, having been commissioned and improved through several small changes in both design and implementation. The flight system has been manufactured and assembled, and is now in an advanced state of testing. The cryogenic system is based on the very successful XQC sounding rocket refrigerator, which provided a low risk starting point for the development of the Micro-X cryostat. Several key areas were redesigned to fulfill the unique requirements of the TESs and MUX readout.
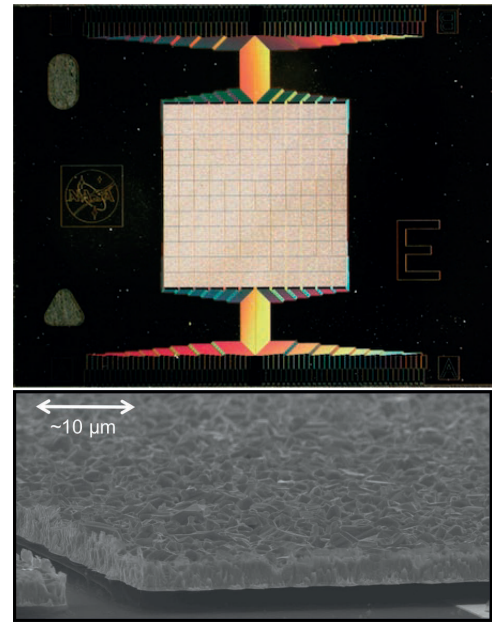
2.6.1 The Micro-X Cryostat

The Micro-X cryostat houses the detector array and the SQUID readout. It provides a stable heat sink for the detector array at a temperature of 50 mK. The entire system is pre-cooled with a pumped liquid He bath. The liquid He bath also serves as a heat intercept at a temperature of 1.6 K. Cooling to the detector array's operating temperature of 50 mK is achieved with a single stage ADR. Photos and a CAD rendering of the Micro-X cryostat are shown in Figures 4 and 7, respectively.

The He tank has a volume of 6 liters and a hold time of nearly 13 hours at 1.6 K, which is considerably more than what is required for both calibration runs and flight operations. The flight helium tank has been extensively tested. It is suspended by three G10 tubes, which provide stiff mechanical support and a high degree of thermal insulation.

The cold stage of the ADR consists of the salt pill, which contains the paramagnetic refrigerant, the Front End Assembly (FEA) with the detector array, a cold finger for thermal connection between the two, and a mechanical support structure. The salt pill is located inside the bore of a 4 T superconducting solenoid magnet. The Ferric-Ammonium-Alum (FAA) salt crystals in the salt pill are grown around several hundred gold wires to provide a good thermal contact to the metal parts of the detector assembly. The first salt pill built for the Micro-X payload reaches base temperatures below 50 mK, and is currently used for laboratory testing. For flight, a new salt pill is being constructed with improved manufacturing techniques, which will lead to hold times at the operating temperature in excess of several hours.

The cold stage is mechanically suspended by Kevlar strings. This suspension system must withstand launch loads, while at the same time conducting very little heat from the He bath to the ADR cold stage. In addition, the Kevlar suspension is part of a three-stage vibration suppression system which keeps mechanical energy from being transmitted from the rocket skin to the detector system during powered flight.[12, 13] Mechanical tests showed the current design can withstand 20 times the expected launch

Figure 7. Cross section of the Micro-X cryostat and the ADR insert. Pictures of the fabricated hardware are shown in Figure 4.

loads. The magnet, part of the suspension system and the salt pill can be seen in Figure 4e. The dewar is attached to the rocket skin using shock mounts with a 40 Hz resonant frequency. The G10 support of the He tank has been designed to resonate at 100 Hz, and the Kevlar suspended detector system at frequencies above 300 Hz. The recent vibration tests to measure these design frequencies was discussed in Section 2.1.

The ADR control electronics have been provided by our collaborators at Wisconsin from a spare set of the XQC sounding rocket electronics. The XQC system has demonstrated ±210 nK RMS temperature stability at 60 mK within 10 s of re-enabling temperature regulation.[14] This is an order of magnitude better than the stability required by the TES detector system. This system has been bench-top tested and is awaiting integration with the flight dewar at MIT.
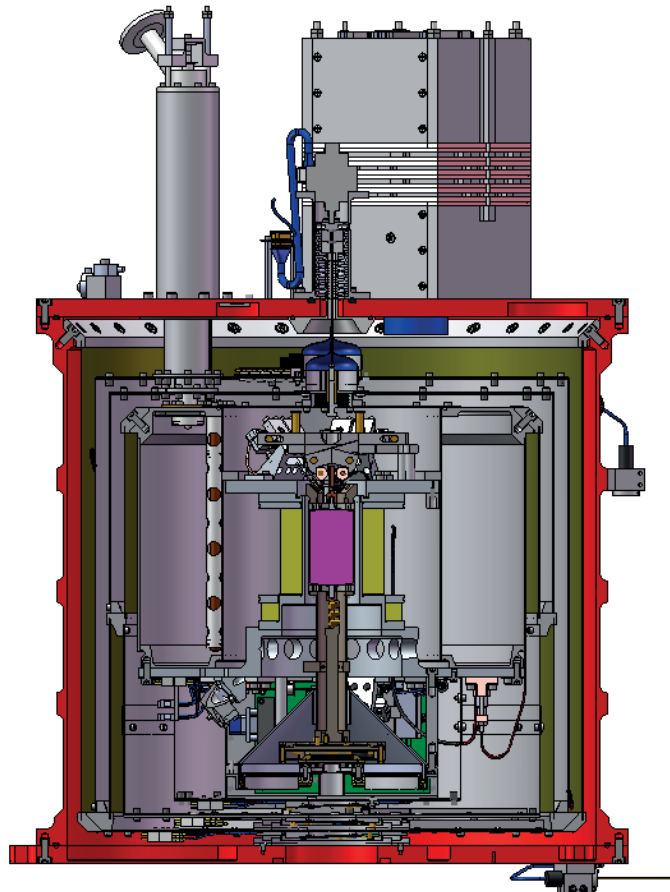
Since TESs are sensitive to magnetic fields, the detector array has to be well shielded from the magnetic field generated by the ADR's magnet. We have designed the ADR to the requirement that the maximum field at the detector array must not exceed 100 nT while the microcalorimeters are operating. This is achieved by distancing the detectors from the magnet by a few inches, incorporating an active "bucking coil" in the magnet design which lowers the field in the region where the detectors reside, and incorporating a very light-weight passive magnetic shield. The passive magnetic shield is made of niobium with an inner lining of high-permeability Metglas material. The niobium, superconducting at the bath operating temperature of 1.5 K, expels magnetic fields interior to the can due to the Meissner-Ochsenfeld effect. The Metglas directs any trapped flux remaining on the inside away from the TESs. Initial 2D finite-element analysis of our original design predicted excellent shielding, however we observed poor performance in the lab. After some study it was determined that 3D asymmetries had to be taken into account in the shield design. Several design improvements were demonstrated to work and are implemented in the current shield, seen in Figure 4g.

2.6.2 The Front End Assembly

The Front End Assembly (FEA) houses the TES microcalorimeter array, the first two SQUID stages of the time-division multiplexer and two germanium resistance thermometers (GRTs), used to measure the temperature of the FEA. Either GRT can be used for temperature control during operation of the instrument. The FEA is mounted on the ADR's cold stage as described in section 2.6.1 above. Since the mass of the cold stage has to be kept low, the components inside the FEA are mounted on a gold-plated lightweight magnesium structure, which forms the base of the focal plane. Figure 8 shows the Micro-X focal plane with its two independent read-out chains.

The detector chip and the interface chips with the SQUID stages each rest on three small tungsten carbide balls. Beryllium-copper clips press the chips against each support ball with a force of 0.16 N. The Si chips are shaped such that this mounting scheme is kinematic, which ensures that the chips are not subjected to any stress resulting from the different thermal expansion coefficients of Si and Mg. Heat sinking of the chips is performed with gold wire bonds, which thermally couple the silicon substrate to the magnesium base plate.

Electrical connections to the detector array, the SQUID stages and the thermometers are made through two superconducting ribbon cables. The entire focal plane is covered by a Mg lid. X-rays reach the TES array through infrared filters described below.
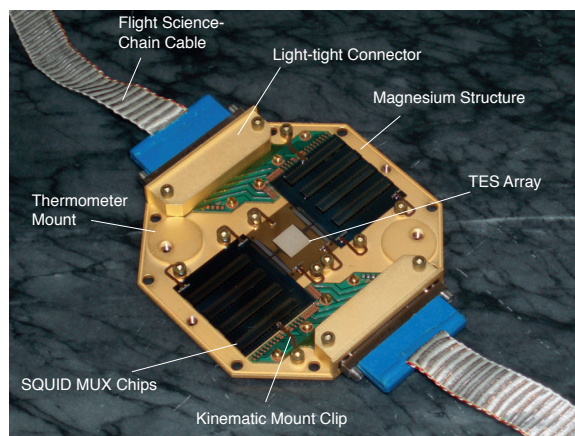
Figure 8. The Micro-X Front End Assembly (FEA).

2.6.3 Calibration Source

In-flight gain calibration is achieved by positioning an on-board source with known line energies in front of the detector array. The source is located inside the superconducting shield within the cryostat. These calibration lines (2.6 and 3.3 keV) are produced by fluorescing a KCl target using an ^{55}Fe source. The calibration source has been successfully assembled and calibrated with a CCD detector at MIT. A 0.1 mm thick layer of aluminized mylar is used to stop electrons (released from the KCl due to the photoelectric effect) from reaching the detector.

2.6.4 Blocking Filters

A stack of 5 thin filters is required in the cryostat aperture to block visible and infrared radiation from the TESs, while allowing X-rays to pass through. The filters are located at different temperature stages on the cryostat. We use the same proven design that flew on the latest XQC flight. Filters will consist of 20 nm of aluminum deposited on a 50 nm thick polyimide film. These are both deposited on a silicon filter holder with monolithic silicon two-level meshes which lend support to the thin films. Fabrication of the flight filters is underway, and a calibration setup and analysis pipeline has been established at MIT with engineering filters.

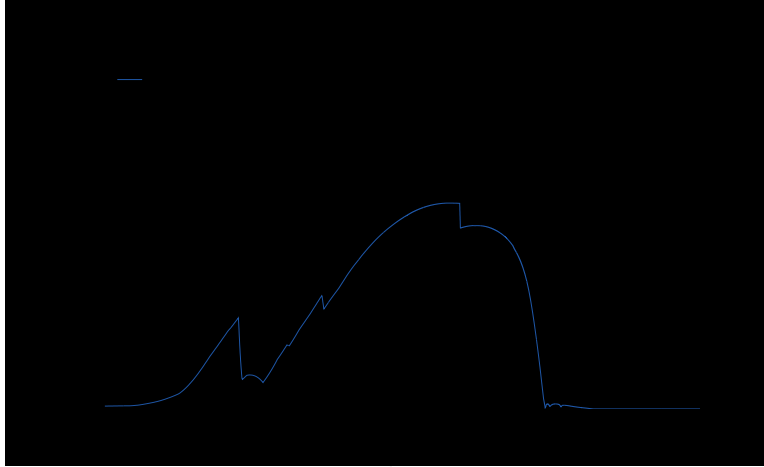Figure 9. Effective area curve for the mirror and filter optical system. The optics module for flights 1 and 2 is shown in black, while the high-resolution optics module for future flights is shown in blue.

2.7 Mirror and Optical Bench

For the first two flights of Micro-X, the X-ray optics module from the Supernova X-Ray Spectrometer (SXS) rocket payload (a GSFC sounding rocket instrument launched in 1988 to observe SN 1987A) will be reused. The module was retrofitted with trimmed spare reflector foils from the Astro-E2 project, and were assembled and tested in the X-ray Optics Lab at the NASA Goddard Space Flight Center. Each quadrant was calibrated optically. Subsequent tests on an X-ray beamline resulted in a measured half power diameter (HPD) of 2.4′.

After X-ray testing of the quadrants, the whole mirror was assembled for the adjustment of the focal point convergence and optical axes parallelism. The focal points of the quadrants converge within an area of 0.1 mm^2 at a focal length of 2100 ± 5 mm, and the optical axes were aligned within ± 0.5 arcmin. A quadrant of the mirror was vibration tested with the Black Brant IX launch excitation spectrum. No significant change in the quadrant's frequency response, image quality or optical axis randomization was measured. The flight-ready mirror is shown in Figure 4d.

The high fill factor of the thin-foil implementation maximizes the effective area obtained within the aperture limitations of a sounding rocket. The measured effective area of the mirror is 300 cm^2 at 1 keV and has a broad energy response (Figure 9). This optics module achieves the desired science goals (see §3.3) while capitalizing on equipment with a proven flight heritage.

The X-ray mirror is held in place by an optical bench made from aluminum beams (Figure 4a). In order to prevent ambient electrons from being focused onto the detectors during flight, a magnetic broom was designed installed on the optical bench. It uses eight Neodymium-iron-boron magnets with a dipole moment of 1.1 A m^2 which effectively shield the detectors from electrons with energies as high as 100 keV.

For future targets our science case will be significantly enhanced by pairing our high spectral resolution detector with a high spatial resolution mirror. Towards this end we have designed a new optics module with five optic shells. These mirrors have a 2.5 meter focal length, a resolution of 30″, and are coated with a layer of rhodium for optimal efficiency over our bandpass (∼0.2–3 keV). These optics are full-shell electroformed nickel replicated (ENR) mirrors.[15, 16] The effective area expected for these optics are also shown in Figure 9.

3. MICRO-X SCIENCE

3.1 Scientific Goals and Objectives

Much of the detailed physics of astronomical sources is accessible only through plasma diagnostics that require moderate to high resolution spectroscopy ($E/dE = R \gg 20$). High resolution spectra have long been available at optical and radio wavelengths, but only very recently in the X-ray band, and even then, largely only for bright point sources. For point sources, the Chandra and XMM-Newton grating spectrometers have demonstrated

the power of $R \gg 20$ spectroscopy in X-rays,[17] ranging from measuring precise chemical abundances in stellar coronae,[18] to solidifying the cooling flow mystery in clusters of galaxies,[19] and uncovering massive outflowing winds in active galaxies.[20] The dispersive nature of the high resolution spectrometers on Chandra and XMM-Newton have sharply limited their use for sources with any significant angular extent. At best, the XMM RGS spectra are an improvement over moderate resolution CCD spectrometers only if a source is more compact than $3'$. Thus, virtually all of the brightest extended sources in the sky are inaccessible for detailed study at the highest spectral resolution. It is this gap that will be filled by Micro-X.

The tremendous scientific potential of high-resolution spectroscopy is well established.[17] For Micro-X, we will focus primarily on two general scientific goals:

- Study the velocity structure of the emitting gas as imprinted in line energy shifts and line profiles.
- Perform plasma line diagnostics to constrain the properties of the plasma and enable inferences regarding its temperature structure, ionization state and element abundances. We target the He-like triplets (these provide strong constraints on the electron density, temperature, and ionization conditions) and the Fe L emission line forest at energies between 0.7–1.4 keV (these dominate collisionally ionized solar-abundance plasmas and provide powerful temperature diagnostics).

3.2 First Flight Science: Observing the Bright Eastern Knot of Puppis A

The first two flights of the Micro-X payload will target the bright, middle-aged galactic SNR Puppis A. This remnant was identified as the product of a core-collapse explosion on the basis of fast-moving optical knots highly enriched in O.[21] The subsequent discovery of a neutron star associated with the remnant,[22] measurement of its high-velocity proper motion,[23] and the recent measurement of its rotation period[24] confirm the core-collapse origin of Puppis A and add to its interest. Thirty years ago, Puppis A was the target of one of the earliest successful high-resolution X-ray spectral observations with the Einstein Focal Plane Crystal Spectrometer.[25–27] The observations were of limited energy range and sensitivity, and the spectra obtained were integrated over the $3' \times 30'$ aperture size. Even so, these observations showed that Puppis A is a bright source of X-ray emission lines of O and Ne.

As a middle-aged remnant, Puppis A straddles the division between young objects whose X-ray emissions are dominated by their supernova debris, or ejecta, and older remnants that have lost all trace of their ejecta. In spite of its estimated age of 4000 years, Puppis A is one of only a handful of remnants that shows fast-moving ejecta in optical emission. Puppis A also shows evidence for X-ray emitting ejecta, with even the earliest Einstein observations suggesting an overall O abundance enhancement.[25, 26] The CCDs on the ASCA X-ray Observatory showed that Ne is particularly enhanced in the fainter western and southern regions of the remnant,[29] and Chandra observations near a complex of shocked interstellar clouds known as the Bright Eastern Knot also showed regions of localized abundance enhancement.[28]

O and Ne ejecta are the unmistakable signature of massive progenitors that synthesize these elements hydrostatically during their lifetimes before the supernova explosion, while much of the Si ejecta was synthesized explosively during the supernova itself. The abundance profile of all the elements in the ejecta help to constrain the properties of the supernova progenitor, but it is the explosively synthesized ejecta such as Si and Fe deep in the core of the exploding star that have the greatest potential to shed light on the supernova explosion itself. This makes the identification of Si-emitting ejecta particularly interesting.

The focus of the Micro-X observation of the bright eastern knot (BEK), in the SNR Puppis A, is to study the physics of a shock front interacting with very dense clouds of material, expanding on previous work.[28] The atomic emission line information gathered with Micro-X will compliment the observational studies performed with *Chandra* and other instruments, and further our understanding of the characteristics of shocks in dense environments. Micro-X will provide new tools to characterize the properties of shocks, such as their velocity, and those of the plasma, including its density profile and post-shock temperature, through the study of thermal X-ray emission. The complex interactions taking place at the BEK may also lead to the first solid detection of charge exchange processes outside of the solar system. Figure 10 shows a simulation of a Micro-X BEK observation fitting the Chandra BEK data to a model including charge exchange,[30] then fitting that fake data with a VNEI model without any charge exchange. As seen in the figure, the assumption of charge exchange clearly changes

the observed Micro-X spectrum, and we expect our BEK observation to either find charge exchange or place strong limits on its existence at the BEK.

One of the key outstanding issues in SNR science is the connection between these objects and cosmic-ray (CR) acceleration. Cosmic-ray hadrons are believed to carry away a significant fraction of the explosion energy and distribute it across the Galaxy, yet we still lack clear evidence of their production in SNRs, as well as a detailed understanding of the acceleration process and its effects on the SNR plasma. The particle acceleration process at the shocks of SNRs is expected to modify the hydrodynamic evolution of the object and the properties of its thermal X-ray emission.[31] Thus, the Micro-X observation of the thermal X-ray emission will provide a new window toward our understanding of the mechanism of cosmic ray production, evidenced by the γ-ray emission detected in the direction of the remnant, and how it couples to the properties of the surrounding material and the shock.

The characteristics of the thermal X-ray emission from SNRs detected in γ-rays have been used successfully to gain insight into the cosmic ray acceleration process. Studies of the hydrodynamic evolution and the properties of the shocked medium and ejecta have yielded important information about CR production. The X-ray morphol-

Figure 10. Simulated BEK observation with Micro-X assuming the existence of charge exchange. The Chandra BEK data[28] was fit using an absorbed variable-abundance non-equilibrium ionization plasma (VNEI) model and an absorbed VNEI + VACX (variable abundance charge exchange) model. The "faked" data is from the VNEI + VACX fit, while the red line is the VNEI-only model. There are clear incompatibilities between the two models, demonstrating that Micro-X should be able to detect charge exchange in the BEK if it is present or place strong limits on its existence.

ogy of Tycho's SNR and SN 1006 indicates that the shock compression ratios in these objects have been modified by the acceleration of cosmic ray ions,[32,33] while comparisons of the postshock plasma temperatures and shock velocities observed in SNRs 1E 0102.2-7219 and RCW 86 also point to a significant fraction of their explosion energy being placed in relativistic particles.[34,35] Most recently, hydrodynamic simulations of SNRs which include particle acceleration at the shock self-consistently, and calculate and track the non-equilibrium state of the post-shock plasma through the evolution of the system, have used thermal X-ray emission as a key diagnostic in understanding the observed broadband properties of some remnants. Such modeling and X-ray line emission observed with the *XMM-Newton* EPIC cameras has been used[36] to conclude that the γ-ray emission detected with the *Fermi* Large Area Telescope (LAT) in the direction of SNR CTB 109 is the result of a combination of emission from accelerated leptons and hadrons. Ellison[37] instead used the lack of line emission observed in RX J1713.7-3946 as a constraint in their modeling, which suggests that its γ-ray emission is dominated by inverse Compton radiation.

The bright eastern knot (BEK) in the SNR Puppis A represents an excellent laboratory for the study of the interaction between SNRs and dense clouds of gas. Cosmic rays interacting with regions of high-density material are expected to result in γ-ray emission from the decay of pions generated by proton-proton interactions. Hence, studying a region of an SNR that appears to be propagating into a molecular or atomic cloud complex is particularly important when searching for signatures of CR acceleration, and in particular, clear signals of hadronic emission. While TeV and GeV observations have revealed γ-ray emission from several SNR-molecular cloud systems,[38–40] X-ray emission from these objects is characterized by a centrally peaked morphology. Recently,
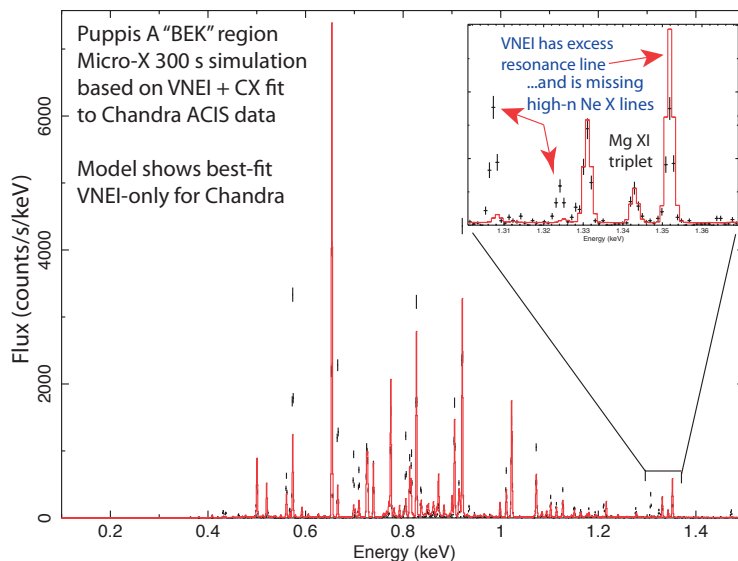
observations with the *Fermi*-LAT revealed an unresolved γ-ray source, with detection significance $> 14\sigma$, with emission centered on the eastern part of the Puppis A remnant. While the study of this region is ongoing, recent preliminary work by our team suggests these γ-rays originate from cosmic ray hadrons accelerated at the shock which are interacting with extremely dense material with which the shock is interacting.

A *Chandra* ACIS observation (see the left inset in Figure 1) allowed a spatially resolved spectral study of the BEK.[28] Using CCD-spectra, maps of temperature and abundance ratios of O and Ne were constructed to illustrate variations in the nature and conditions of the shocked material in this area. Additionally, the high-spatial resolution of *Chandra* revealed substructures in the shock-heated gas, which are somewhat similar to those observed in laboratory laser experiments designed to model such conditions.[28,41] Hence, these studies identified cloud-shock interaction in a relatively mature stage of evolution.

The elements observed by *Chandra* and *XMM-Newton*–O, Ne, Mg, Si, and Fe–in the BEK have strong lines well suited to be studied with Micro-X. The *Chandra* study of the region reveal structures on angular scales smaller than $1'$. However, the main morphological features appear to have sizes which are well-matched by the modest angular resolution of the first Micro-X mirror and its field of view. Simulation based on the *Chandra* spectrum of the entire knot gives about 27,000 counts in a 300 s Micro-X observation. The objectives of the Micro-X observation of the BEK are: (1) use line broadening and ratios to obtain information about the dynamics of elements in different regions of the shocked high-density cloud complex; and (2), use plasma diagnostics for the various emission lines of each element to establish variations in the thermodynamic conditions of different elements across the interaction region. Meeting these goals, we will be able to characterize the interaction region between an SNR and a high-density cloud complex with spatially resolved high-resolution X-ray spectra for the first time, and gain crucial insight into the nature of such systems, obtaining a very clear picture of the conditions in a region where cosmic ray acceleration is known to be taking place.

3.3 Second Flight Science: Puppis A Ejecta Knot

The improved sensitivity and spectral resolution of the CCDs on the Suzaku X-ray Observatory have led to the identification of a coherent, large-scale ejecta feature in "equivalent width", or line/continuum images, of Si emission in Puppis A,[2] Figure 1(right inset). This roughly $8' \times 10'$ region is located in the north/northeast region of the remnant, somewhat farther out in radius than the optically-identified O ejecta. Much of the imprint of the supernova explosion that formed Puppis A has been lost in the intervening 4000 years, but the fragments of debris originating from deep within the star still hold valuable clues to understand the explosion.

The high velocities of the optically emitting ejecta (1500 km/s) and the high velocity recoil of the neutron star (also $\sim$1500 km/s) suggest that X-ray emitting ejecta should also have high velocities. Indeed, XMM-Newton observations of a small region corresponding to a bright optical ejecta feature known as the Ω knot (located at the southeastern edge of our target Si ejecta knot within our FOV[42]) show evidence for blueshifted emission lines corresponding to velocities of 1500-3000 km/s. They also show evidence for temperature and abundance differences on $1'$ angular scales. The Suzaku observations show that the large ejecta knot can be subdivided into two parts, with the northern half dominated more strongly by Mg and Si than the southern half, in which the O and Ne emission are relatively stronger. The element abundance maps obtained by Suzaku confirm that this entire feature is enhanced not only in Si, but also in O, Ne, Mg, and possibly Fe.

All of the ejecta elements observed by Suzaku and XMM-Newton–O, Ne, Mg, Si, and Fe–have strong lines that will be accessible to Micro-X. While Chandra observations of the region do show that there is some structure on smaller angular scales, this $8' \times 10'$ feature is overall well-matched to the modest angular resolution of the initial Micro-X mirror and its field of view. A simulation based on the spectrum observed by Suzaku for the entire knot yields about 17,000 counts in a 300 s Micro-X observation (Figure 1).

The goals of our Micro-X observation of the Si ejecta knot in Puppis A are to:

- Search for velocity shifts in the various emission lines and measure the line structures to obtain information about the dynamics of the various ejecta elements.
- Perform plasma diagnostics for the various emission lines of individual elements to ascertain how similar or different the thermodynamic states of the various elements are.
- Refine estimates of element abundances in the ejecta.

Velocity and dynamics will give us direct information as to how well-mixed the ejecta are, and in particular, whether there were any differences in the dynamics of the outlying O and Ne ejecta compared to the inner Si and Fe ejecta. Although velocity shift measurements have been attempted with CCD spectra,[42] those moderate resolution spectra do not resolve individual lines so that the energy shift of any particular line is partly obscured by the presence or absence of weak lines in the blend. This is especially true for supernova remnant plasmas, for which the ionization state of the gas is still evolving toward equilibrium.

At the next level, we will study the thermodynamics of the plasma. The progress to ionization equilibrium depends on both the density of the gas and the shock time, so that the ionization age serves as an important indicator of the evolution of the remnant. Complexities in the temperature structure are also expected, as a range of temperatures is indicated in Chandra, XMM-Newton, and Suzaku observations. In the case of the Fe L lines, the mere identification of the L lines present in the spectrum gives a diagnostic of the range of temperatures in the gas.

Finally, once the dynamic effects and the physical properties of the emitting gas are understood, the high resolution Micro-X spectrum will provide the means to refine estimates of element abundances in the ejecta. The detailed insights into the temperature and ionization structure are crucial to such an effort. Although the ejecta knot is only a relatively small part of the total ejected material, its large physical scale suggests that it may be a fair representation of the whole. The Micro-X observation would then enable a detailed comparison to the nucleosynthesis predicted in core-collapse SN models.

Figure 1(bottom) shows a simulation of the Micro-X spectrum for μX-F1. Many individual lines from different elements are visible. The inset shows the oxygen He-like triplet, with a 1500 km/s blueshifted version in dashed blue, showing the power of Micro-X to both measure the triplet component fluxes and accurately measure line velocities.

4. CONCLUSIONS

The Micro-X payload has been in development for several years and is nearing its first launch date. Our progress has been slowed by a variety of integration issues that are not unheard of in the buildup of such a complex payload. We anticipate a launch in January 2013, with another to follow within a year of the first. Both flights will study the Puppis A supernova remnant, and will begin to deliver on the promise of high-spectral resolution science for extended X-ray sources.

5. ACKNOWLEDGEMENTS

REFERENCES

1. S. Katsuda, U. Hwang, R. Petre, S. Park, K. Mori, and H. Tsunemi, "Discovery of X-ray-emitting O-Ne-Mg-rich Ejecta in the Galactic Supernova Remnant Puppis A," *ApJ* **714**, pp. 1725–1732, May 2010.

2. U. Hwang, R. Petre, and K. A. Flanagan, "X-Ray-emitting Ejecta in Puppis A Observed with Suzaku," *ApJ* **676**, pp. 378–389, Mar. 2008.

3. N. Iyomoto, S. R. Bandler, R. P. Brekosky, A.-D. Brown, J. A. Chervenak, F. M. Finkbeiner, R. L. Kelley, C. A. Kilbourne, F. S. Porter, J. E. Sadleir, S. J. Smith, and E. Figueroa-Feliciano, "Close-packed arrays of transition-edge x-ray microcalorimeters with high spectral resolution at 5.9 keV," *Applied Physics Letters* **92**, p. 3508, Jan. 2008.

4. S. R. Bandler, R. P. Brekosky, A.-D. Brown, J. A. Chervenak, E. Figueroa-Feliciano, F. M. Finkbeiner, N. Iyomoto, R. L. Kelley, C. A. Kilbourne, F. S. Porter, J. Sadleir, and S. J. Smith, "Performance of TES X-ray Microcalorimeters with a Novel Absorber Design," *Journal of Low Temperature Physics* **151**, pp. 400–405, Apr. 2008.

5. M. E. Eckart, J. S. Adams, C. N. Bailey, S. R. Bandler, S. E. Busch, J. A. Chervenak, F. M. Finkbeiner, R. L. Kelley, C. A. Kilbourne, F. S. Porter, J. P. Porst, J. E. Sadleir, and S. J. Smith, "Kilopixel X-ray Microcalorimeter Arrays for Astrophysics: Device Performance and Uniformity," *Journal of Low Temperature Physics* **167**, pp. 732–740, June 2012.

6. S. J. Smith, J. S. Adams, C. N. Bailey, S. R. Bandler, J. A. Chervenak, M. E. Eckart, F. M. Finkbeiner, R. L. Kelley, C. A. Kilbourne, F. S. Porter, and J. E. Sadleir, "Small Pitch Transition-Edge Sensors with Broadband High Spectral Resolution for Solar Physics," *Journal of Low Temperature Physics* **167**, pp. 168–175, May 2012.

7. P. A. J. de Korte, J. Beyer, S. Deiker, G. C. Hilton, K. D. Irwin, M. Macintosh, S. W. Nam, C. D. Reintsema, L. R. Vale, and M. E. Huber, "Time-division superconducting quantum interference device multiplexer for transition-edge sensors," *Review of Scientific Instruments* **74**, pp. 3807–3815, Aug. 2003.

8. K. D. Irwin, M. D. Audley, J. A. Beall, J. Beyer, S. Deiker, W. Doriese, W. Duncan, G. C. Hilton, W. Holland, C. D. Reintsema, J. N. Ullom, L. R. Vale, and Y. Xu, "In-focal-plane SQUID multiplexer," *Nuclear Instruments and Methods in Physics Research A* **520**, pp. 544–547, Mar. 2004.

9. C. D. Reintsema, J. Beyer, S. W. Nam, S. Deiker, G. C. Hilton, K. Irwin, J. Martinis, J. Ullom, L. R. Vale, and M. Macintosh, "Prototype system for superconducting quantum interference device multiplexing of large-format transition-edge sensor arrays," *Review of Scientific Instruments* **74**, pp. 4500–4508, Oct. 2003.

10. R. P. Welty and J. M. Martinis, "A series array of dc squids," *IEEE Trans. Magn* **27**, pp. 2924–2926, 1991.

11. R. P. Welty and J. M. Martinis, "Two-stage integrated SQUID amplifier with series array output," *IEEE Transactions on Applied Superconductivity* **3**, pp. 2605–2608, Mar. 1993.

12. W. Cui, R. Almy, S. Deiker, D. McCammon, J. Morgenthaler, W. T. Sanders, R. L. Kelley, F. E. Marshall, S. H. Moseley, C. K. Stahle, and A. E. Szymkowiak, "Sounding rocket experiment employing microcalorimeter detectors to obtain a high-resolution spectrum of the diffuse x-ray background," in *Proc. SPIE Vol. 2280, p. 362-373, EUV, X-Ray, and Gamma-Ray Instrumentation for Astronomy V, Oswald H. Siegmund; John V. Vallerga; Eds.*, O. H. Siegmund and J. V. Vallerga, eds., pp. 362–373, Sept. 1994.

13. P. Wikus, J. S. Adams, Y. Bagdasarova, S. R. Bandler, W. B. Doriese, M. E. Eckart, E. Figueroa-Feliciano, R. L. Kelley, C. A. Kilbourne, S. W. Leman, D. McCammon, F. S. Porter, J. M. Rutherford, and S. N. Trowbridge, "The Adiabatic Demagnetization Refrigerator for the Micro-X Sounding Rocket Telescope," in *American Institute of Physics Conference Series*, J. G. Weisend, ed., *American Institute of Physics Conference Series* **1218**, pp. 633–640, Apr. 2010.

14. D. McCammon, R. Almy, E. Apodaca, W. Bergmann Tiest, W. Cui, S. Deiker, M. Galeazzi, M. Juda, A. Lesser, T. Mihara, J. P. Morgenthaler, W. T. Sanders, J. Zhang, E. Figueroa-Feliciano, R. L. Kelley, S. H. Moseley, R. F. Mushotzky, F. S. Porter, C. K. Stahle, and A. E. Szymkowiak, "A high spectral resolution observation of the soft x-ray diffuse background with thermal detectors," *ApJ* **576**, pp. 188–203, 2002.

15. B. Ramsey and P. Gorenstein, "A hard x-ray telescope science enhancement package for the Constellation X-Ray mission," in *Society of Photo-Optical Instrumentation Engineers (SPIE) Conference Series*, **6688**, Sept. 2007.

16. B. D. Ramsey, "Replicated nickel optics for the hard-x-ray region," *Experimental Astronomy* **20**(1), pp. 85–92, 2005.

17. F. B. S. Paerels and S. M. Kahn, "High-Resolution X-Ray Spectroscopy with CHANDRA and XMM-NEWTON," *ARA&A* **41**, pp. 291–342, 2003.

18. M. Güdel, M. Audard, F. Reale, S. L. Skinner, and J. L. Linsky, "Flares from small to large: X-ray spectroscopy of Proxima Centauri with XMM-Newton," *A&A* **416**, pp. 713–732, Mar. 2004.

19. J. R. Peterson, S. M. Kahn, F. B. S. Paerels, J. S. Kaastra, T. Tamura, J. A. M. Bleeker, C. Ferrigno, and J. G. Jernigan, "High-Resolution X-Ray Spectroscopic Constraints on Cooling-Flow Models for Clusters of Galaxies," *ApJ* **590**, pp. 207–224, June 2003.

20. D. M. Crenshaw, S. B. Kraemer, and I. M. George, "Mass Loss from the Nuclei of Active Galaxies," *ARA&A* **41**, pp. 117–167, 2003.

21. P. F. Winkler and R. P. Kirshner, "Discovery of fast-moving oxygen filaments in Puppis A," *ApJ* **299**, pp. 981–986, Dec. 1985.

22. R. Petre, C. M. Becker, and P. F. Winkler, "A Central Stellar Remnant in Puppis A," *ApJL* **465**, pp. L43+, July 1996.

23. P. F. Winkler and R. Petre, "Direct Measurement of Neutron Star Recoil in the Oxygen-rich Supernova Remnant Puppis A," *ApJ* **670**, pp. 635–642, Nov. 2007.

24. E. V. Gotthelf and J. P. Halpern, "Discovery of a 112 ms X-ray Pulsar in Puppis A: Further Evidence of Neutron Stars Weakly Magnetized at Birth," *ArXiv e-prints* , Feb. 2009.

25. K. A. Flanagan, "Plasma Diagnostics with X-Ray Emission Lines of Puppis A.," *MIT Ph.D. Thesis* , 1990.

26. C. R. Canizares and P. F. Winkler, "Evidence for elemental enrichment of Puppis A by a Type II supernova," *ApJL* **246**, pp. L33–L36, May 1981.

27. P. F. Winkler, G. W. Clark, T. H. Markert, K. Kalata, H. W. Schnopper, and C. R. Canizares, "A survey of X-ray line emission from the supernova remnant Puppis A," *ApJL* **246**, pp. L27–L31, May 1981.

28. U. Hwang, K. A. Flanagan, and R. Petre, "Chandra X-Ray Observation of a Mature Cloud-Shock Interaction in the Bright Eastern Knot Region of Puppis A," *ApJ* **635**, pp. 355–364, Dec. 2005.

29. K. Tamura, "ASCA observation of the Puppis A supernova remnant," *Ph.D. Thesis* , 1994.

30. R. K. Smith, A. R. Foster, and N. S. Brickhouse, "Approximating the X-ray spectrum emitted from astrophysical charge exchange," *Astronomische Nachrichten* **333**, p. 301, 2012.

31. D. Castro, P. Slane, D. J. Patnaude, and D. C. Ellison, "The Impact of Efficient Particle Acceleration on the Evolution of Supernova Remnants in the Sedov-Taylor Phase," *ApJ* **734**, p. 85, June 2011.

32. J. S. Warren, J. P. Hughes, C. Badenes, P. Ghavamian, C. F. McKee, D. Moffett, P. P. Plucinsky, C. Rakowski, E. Reynoso, and P. Slane, "Cosmic-Ray Acceleration at the Forward Shock in Tycho's Supernova Remnant: Evidence from Chandra X-Ray Observations," *ApJ* **634**, pp. 376–389, Nov. 2005.

33. G. Cassam-Chenaï, J. P. Hughes, E. M. Reynoso, C. Badenes, and D. Moffett, "Morphological Evidence for Azimuthal Variations of the Cosmic-Ray Ion Acceleration at the Blast Wave of SN 1006," *ApJ* **680**, pp. 1180–1197, June 2008.

34. J. P. Hughes, C. E. Rakowski, and A. Decourchelle, "Electron Heating and Cosmic Rays at a Supernova Shock from Chandra X-Ray Observations of 1E 0102.2-7219," *ApJL* **543**, pp. L61–L65, Nov. 2000.

35. E. A. Helder, J. Vink, C. G. Bassa, A. Bamba, J. A. M. Bleeker, S. Funk, P. Ghavamian, K. J. van der Heyden, F. Verbunt, and R. Yamazaki, "Measuring the Cosmic-Ray Acceleration Efficiency of a Supernova Remnant," *Science* **325**, pp. 719–, Aug. 2009.

36. D. Castro, P. Slane, D. C. Ellison, and D. J. Patnaude, "Fermi-LAT Observations and A Broadband Study of Supernova Remnant CTB 109," *Submitted to The Astrophysical Journal* , Jan. 2012.

37. D. C. Ellison, D. J. Patnaude, P. Slane, and J. Raymond, "Efficient Cosmic Ray Acceleration, Hydrodynamics, and Self-Consistent Thermal X-Ray Emission Applied to Supernova Remnant RX J1713.7-3946," *ApJ* **712**, pp. 287–293, Mar. 2010.

38. F. Aharonian, A. G. Akhperjanian, A. R. Bazer-Bachi, M. Beilicke, W. Benbow, D. Berge, K. Bernlöhr, C. Boisson, O. Bolz, V. Borrel, I. Braun, F. Breitling, A. M. Brown, P. M. Chadwick, L.-M. Chounet, R. Cornils, L. Costamante, B. Degrange, H. J. Dickinson, A. Djannati-Ataï, L. O. Drury, G. Dubus, D. Emmanoulopoulos, P. Espigat, F. Feinstein, G. Fontaine, Y. Fuchs, S. Funk, Y. A. Gallant, B. Giebels, S. Gillessen, J. F. Glicenstein, P. Goret, C. Hadjichristidis, M. Hauser, G. Heinzelmann, G. Henri, G. Hermann, J. A. Hinton, W. Hofmann, M. Holleran, D. Horns, A. Jacholkowska, O. C. de Jager, B. Khélifi, N. Komin, A. Konopelko, I. J. Latham, R. Le Gallou, A. Lemière, M. Lemoine-Goumard, N. Leroy, T. Lohse, J. M. Martin, O. Martineau-Huynh, A. Marcowith, C. Masterson, T. J. L. McComb, M. de Naurois, S. J. Nolan, A. Noutsos, K. J. Orford, J. L. Osborne, M. Ouchrif, M. Panter, G. Pelletier, S. Pita, G. Pühlhofer, M. Punch, B. C. Raubenheimer, M. Raue, J. Raux, S. M. Rayner, A. Reimer, O. Reimer, J. Ripken, L. Rob, L. Rolland, G. Rowell, V. Sahakian, L. Saugé, S. Schlenker, R. Schlickeiser, C. Schuster, U. Schwanke, M. Siewert, H. Sol, D. Spangler, R. Steenkamp, C. Stegmann, J.-P. Tavernet, R. Terrier, C. G. Théoret, M. Tluczykont, G. Vasileiadis, C. Venter, P. Vincent, H. J. Völk, and S. J. Wagner, "The H.E.S.S. Survey of the Inner Galaxy in Very High Energy Gamma Rays," *ApJ* **636**, pp. 777–797, Jan. 2006.

39. A. A. Abdo, M. Ackermann, M. Ajello, L. Baldini, J. Ballet, G. Barbiellini, M. G. Baring, D. Bastieri, B. M. Baughman, K. Bechtol, R. Bellazzini, B. Berenji, R. D. Blandford, E. D. Bloom, E. Bonamente, A. W. Borgland, A. Bouvier, J. Bregeon, A. Brez, M. Brigida, P. Bruel, T. H. Burnett, S. Buson, G. A. Caliandro, R. A. Cameron, P. A. Caraveo, J. M. Casandjian, C. Cecchi, Ö. Çelik, A. Chekhtman, C. C. Cheung, J. Chiang, S. Ciprini, R. Claus, J. Cohen-Tanugi, L. R. Cominsky, J. Conrad, S. Cutini, C. D. Dermer,

A. de Angelis, F. de Palma, S. W. Digel, M. Dormody, E. d. C. e. Silva, P. S. Drell, R. Dubois, D. Dumora, C. Farnier, C. Favuzzi, S. J. Fegan, W. B. Focke, P. Fortin, M. Frailis, Y. Fukazawa, S. Funk, P. Fusco, F. Gargano, D. Gasparrini, N. Gehrels, S. Germani, G. Giavitto, B. Giebels, N. Giglietto, F. Giordano, T. Glanzman, G. Godfrey, I. A. Grenier, M.-H. Grondin, J. E. Grove, L. Guillemot, S. Guiriec, Y. Hanabata, A. K. Harding, M. Hayashida, E. Hays, R. E. Hughes, M. S. Jackson, G. Jóhannesson, A. S. Johnson, T. J. Johnson, W. N. Johnson, T. Kamae, H. Katagiri, J. Kataoka, J. Katsuta, N. Kawai, M. Kerr, J. Knödlseder, M. L. Kocian, M. Kuss, J. Lande, L. Latronico, M. Lemoine-Goumard, F. Longo, F. Loparco, B. Lott, M. N. Lovellette, P. Lubrano, A. Makeev, M. N. Mazziotta, J. E. McEnery, C. Meurer, P. F. Michelson, W. Mitthumsiri, T. Mizuno, A. A. Moiseev, C. Monte, M. E. Monzani, A. Morselli, I. V. Moskalenko, S. Murgia, T. Nakamori, P. L. Nolan, J. P. Norris, E. Nuss, T. Ohsugi, A. Okumura, N. Omodei, E. Orlando, J. F. Ormes, D. Paneque, D. Parent, V. Pelassa, M. Pepe, M. Pesce-Rollins, F. Piron, T. A. Porter, S. Rainò, R. Rando, M. Razzano, A. Reimer, O. Reimer, T. Reposeur, S. Ritz, A. Y. Rodriguez, R. W. Romani, M. Roth, F. Ryde, H. F.-W. Sadrozinski, D. Sanchez, A. Sander, P. M. Saz Parkinson, J. D. Scargle, T. L. Schalk, C. Sgrò, E. J. Siskind, D. A. Smith, P. D. Smith, G. Spandre, P. Spinelli, M. S. Strickman, D. J. Suson, H. Tajima, H. Takahashi, T. Takahashi, T. Tanaka, J. B. Thayer, J. G. Thayer, D. J. Thompson, L. Tibaldo, O. Tibolla, D. F. Torres, G. Tosti, A. Tramacere, Y. Uchiyama, T. L. Usher, V. Vasileiou, C. Venter, N. Vilchez, V. Vitale, A. P. Waite, P. Wang, B. L. Winer, K. S. Wood, R. Yamazaki, T. Ylinen, and M. Ziegler, "Fermi LAT Discovery of Extended Gamma-Ray Emission in the Direction of Supernova Remnant W51C," *ApJL* **706**, pp. L1–L6, Nov. 2009.

40. D. Castro and P. Slane, "Fermi Large Area Telescope Observations of Supernova Remnants Interacting with Molecular Clouds," *ApJ* **717**, pp. 372–378, July 2010.

41. R. I. Klein, K. S. Budil, T. S. Perry, and D. R. Bach, "The Interaction of Supernova Remnants with Interstellar Clouds: Experiments on the Nova Laser," *ApJ* **583**, pp. 245–259, Jan. 2003.

42. S. Katsuda, K. Mori, H. Tsunemi, S. Park, U. Hwang, D. N. Burrows, J. P. Hughes, and P. O. Slane, "Discovery of Fast-Moving X-Ray-Emitting Ejecta Knots in the Oxygen-Rich Supernova Remnant Puppis A," *ApJ* **678**, pp. 297–302, May 2008.